nature chemistry

ARTICLES

PUBLISHED ONLINE: 12 AUGUST 2012 | DOI: 10.1038/NCHEM.1421

Understanding and controlling the substrate effect on graphene electron-transfer chemistry via reactivity imprint lithography

Qing Hua Wang[1], Zhong Jin[1], Ki Kang Kim[2], Andrew J. Hilmer[1], Geraldine L. C. Paulus[1], Chih-Jen Shih[1], Moon-Ho Ham[3], Javier D. Sanchez-Yamagishi[4], Kenji Watanabe[5], Takashi Taniguchi[5], Jing Kong[2], Pablo Jarillo-Herrero[4] and Michael S. Strano[1]*

Graphene has exceptional electronic, optical, mechanical and thermal properties, which provide it with great potential for use in electronic, optoelectronic and sensing applications. The chemical functionalization of graphene has been investigated with a view to controlling its electronic properties and interactions with other materials. Covalent modification of graphene by organic diazonium salts has been used to achieve these goals, but because graphene comprises only a single atomic layer, it is strongly influenced by the underlying substrate. Here, we show a stark difference in the rate of electron-transfer reactions with organic diazonium salts for monolayer graphene supported on a variety of substrates. Reactions proceed rapidly for graphene supported on SiO_2 and Al_2O_3 (sapphire), but negligibly on alkyl-terminated and hexagonal boron nitride (hBN) surfaces, as shown by Raman spectroscopy. We also develop a model of reactivity based on substrate-induced electron–hole puddles in graphene, and achieve spatial patterning of chemical reactions in graphene by patterning the substrate.

Graphene is a two-dimensional, atomically thin lattice of sp^2-bonded carbon atoms and has exceptional electronic, mechanical and thermal properties[1,2]. Modifying the basic electronic, chemical and structural properties of graphene is important for incorporating graphene into a variety of applications including electronic devices, biosensors and composite materials[3]. The chemical functionalization of graphene is critical for enabling these applications and has been explored for both covalent[4,5] and non-covalent[6–8] schemes. Functionalizing graphene with aryl diazonium salts[4,9–16] results in the opening of a bandgap[10,13,17–19] and shifting of the Fermi level[10], both of which are desirable in the fabrication of electronic devices. In addition, the functional groups on the diazonium moiety can be tailored by organic chemistry to allow various chemical characteristics to be coupled to the graphene[9].

Graphene is strongly influenced by the underlying substrate. SiO_2-covered silicon substrates are compatible with device fabrication, but they have rough surfaces and contain charged impurities. These lead to electron–hole charge fluctuations (or 'puddles') in the graphene, which scatter charge carriers and inhibit electronic device performance[20,21]. Graphene devices suspended over gaps exhibit the highest carrier mobilities[22,23], but are not robust for practical use. Recently, single-crystal hexagonal boron nitride (hBN)[24,25] and self-assembled monolayers (SAMs) of hydrophobic molecules grafted on SiO_2 substrates[26–29] have been explored as alternative substrates for graphene electronics. Graphene on hBN, which is atomically smooth, chemically inert and electrically insulating, has significantly smaller electron–hole charge fluctuations and higher mobilities[24,25]. Graphene devices on SAM-covered substrates also exhibit lower charge inhomogeneity and performance hysteresis[26,27] because the SAMs prevent dipolar contaminants from adsorbing on the substrate, prevent charge injection from the graphene to the dielectric interface and screen the effect of charged impurities within the substrate[26,27,29].

In this Article, we demonstrate that the substrate on which graphene rests strongly influences the chemical reactions on the top surface of the graphene. We also demonstrate spatial control of the chemical reactivity of graphene with micrometre-scale resolution to achieve wafer-scale patterning of chemical reactions on graphene. A previous report has shown differences in reactivity for small mechanically exfoliated flakes of graphene on SiO_2 and hexamethyldisilazane (HMDS)-treated SiO_2 (ref. 30). In the present work, chemical vapour deposition (CVD)-grown graphene is deposited on a variety of substrates and covalently functionalized with aryl diazonium salts. Using Raman spectroscopic mapping, we find that the substrate-induced electron–hole charge fluctuations in graphene greatly influence the chemical reactivity. Graphene on SiO_2 and Al_2O_3 (sapphire) substrates is highly reactive, but graphene on an alkyl-terminated monolayer and hBN is much less reactive. We also develop a new lithographic patterning technique, reactivity imprint lithography (RIL), where the underlying substrate is chemically patterned to achieve spatial control of the graphene chemical reactivity. This method allows chemical reactions on graphene to be spatially patterned over large areas without the use of disruptive materials such as photoresists or chemical etchants. Here, RIL is used to spatially control the conjugation of enhanced green fluorescent protein (EGFP) on graphene, directly from solution, demonstrating the advantages of the technique for producing structures for sensor and microarray applications.

[1]Department of Chemical Engineering, Massachusetts Institute of Technology, Cambridge, Massachusetts 02139, USA, [2]Department of Electrical Engineering and Computer Science, Massachusetts Institute of Technology, Cambridge, Massachusetts 02139, USA, [3]School of Materials Science and Engineering, Gwangju Institute of Science and Technology, Gwangju 500-712, South Korea, [4]Department of Physics, Massachusetts Institute of Technology, Cambridge, Massachusetts 02139, USA, [5]Advanced Materials Laboratory, National Institute for Materials Science, 1-1 Namiki, Tsukuba 305-0044, Japan. *e-mail: strano@mit.edu

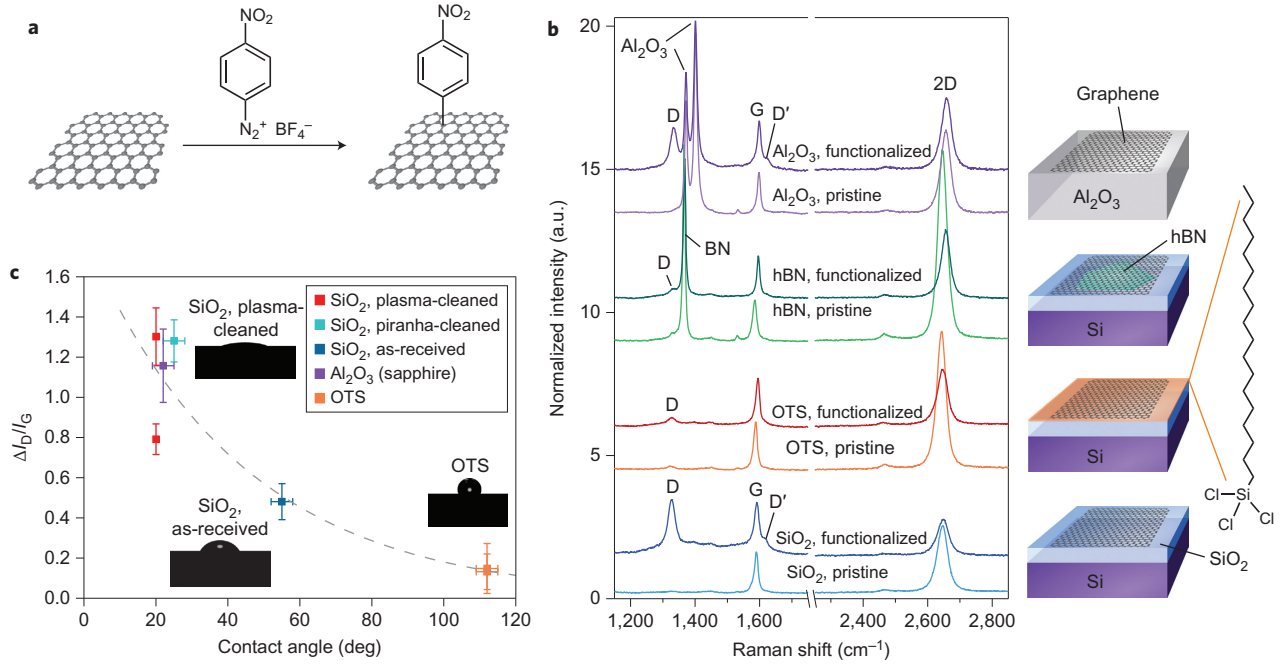

Figure 1 | Chemical reactivity of graphene supported on different substrates. a, Reaction scheme of covalent chemical functionalization of graphene by 4-nitrobenzenediazonium tetrafluoroborate. **b**, Representative Raman spectra of CVD-grown graphene deposited on different substrate materials before and after diazonium functionalization, normalized to the G peak height. These substrates are, from bottom to top, 300-nm-thick SiO_2 on silicon, SiO_2 functionalized by an OTS SAM, single-crystal hBN flakes deposited on SiO_2 and single-crystal α-Al_2O_3 (*c*-face sapphire). The SiO_2 substrate here was plasma-cleaned. **c**, Change in intensity ratio of Raman D and G peaks (I_D/I_G) after diazonium functionalization (difference between functionalized and unfunctionalized ratios) plotted as a function of water contact-angle of the substrate before graphene deposition. The dashed line is an exponential fit of the data. Raman spectra were taken with a laser excitation wavelength of 633 nm.

Results and discussion

Chemical reactivity of graphene on different substrates. Large-area monolayer graphene grown by CVD on copper foils[31] was cut into smaller pieces and transferred onto several different substrates using a poly(methyl methacrylate) (PMMA)-mediated transfer method[32]. Graphene grown by CVD on copper foils is predominantly monolayer, but polycrystalline (Supplementary Figs S1,S2)[33,34]. Covalent functionalization via an electron-transfer reaction with 4-nitrobenzenediazonium (4-NBD) tetrafluoroborate results in nitrobenzene groups being covalently attached to the graphene lattice (Fig. 1a). Figure 1b (right) shows the substrates used in this work: 300-nm-thick SiO_2 on a silicon wafer; a SAM of octadecyltrichlorosilane (OTS) on 300 nm SiO_2; a mechanically exfoliated flake of 90-nm-thick single-crystal hBN deposited on 300 nm SiO_2; and a single-crystal wafer of α-Al_2O_3 (polished sapphire, *c*-plane). The SiO_2 substrate was cleaned by oxygen plasma to generate a hydrophilic surface terminated with –OH groups.

Figure 1b presents representative Raman spectra of graphene on each substrate before and after diazonium functionalization. The primary peaks are the G peak near 1,580 cm^{-1}, the D peak near 1,300–1,350 cm^{-1} and the 2D peak near 2,600–2,700 cm^{-1} (refs 35,36). The G and 2D peaks provide information about the level of doping, strain and layer number[35–38], and the D peak is activated by lattice defects[39] including physical damage[38,40] and the formation of sp^3 hybridization by covalent chemistry[5,10]. The integrated intensity ratio of the D and G peaks (I_D/I_G) is a measure of the concentration of covalent defect sites, and has been used by other researchers to characterize the degree of covalent functionalization[10]. Under our reaction conditions, physical damage is not incurred by the graphene lattice, so the increase in the D peak can be attributed directly to the formation of covalent bonds as a result of diazonium functionalization. In the spectra for pristine graphene in Fig. 1b, which are normalized to the G peak height, the D peak is very small on all substrates and differences are seen in the I_{2D}/I_G ratios. After diazonium functionalization, prominent D peaks and small D′ peaks appear on the SiO_2 and Al_2O_3 substrates, indicating the significant formation of sp^3 bonds. On the OTS and hBN substrates, very small D peaks appear, indicating sparse covalent functionalization. For all substrates, the G and 2D peaks are shifted up in position, and the 2D peak intensity is decreased.

The correlation of chemical reactivity with the hydrophobicity of the underlying substrate is shown in Fig. 1c. In addition to the oxygen-plasma-cleaned bare SiO_2, we studied SiO_2 cleaned by piranha solution (3:1 solution of sulfuric acid and 30% hydrogen peroxide), which also produces a hydrophilic surface, and a sample that was used as received. The hBN flakes were typically under 100 μm in diameter and were too small for macroscopic contact-angle measurements. In general, the contact angle of the substrate appears to be inversely correlated with graphene chemical reactivity. Low contact angles indicate hydrophilicity due to polar chemical groups at the surface, which can induce electron–hole puddles in graphene, whereas high contact angles indicate nonpolar surfaces. Further analysis of Raman spectra was conducted to clarify the role of the substrate in changing the chemical reactivity of graphene.

Analysis of Raman spectroscopic maps. Two-dimensional Raman maps, with 121 spectra each and for points spaced 1 μm apart, were taken in the same 10 μm × 10 μm sample areas before and after diazonium functionalization. The Raman mapping enables a statistical analysis of many spectra and accounts for spatial heterogeneity in the graphene properties across the samples. Regions of uniform monolayer graphene were chosen to avoid bilayer or multilayer islands, wrinkles and edges (see Supplementary Fig. S1 for optical microscope images and additional Raman spectra of the initial graphene). The average peak parameters from fitting the peaks to Lorentzian functions

Table 1 | Summary of graphene Raman peak parameters before and after diazonium functionalization.

	ω_G (cm^{-1})	Γ_G (cm^{-1})	ω_{2D} (cm^{-1})	Γ_{2D} (cm^{-1})	I_D/I_G	I_{2D}/I_G	σ (cm^{-2})
SiO_2, pristine	1,588.6	14.4	2,644.1	33.7	0.11	4.24	7.1×10^{11}
SiO_2, functionalized	1,591.9	18.1	2,649.8	36.1	1.42	1.64	1.1×10^{13}
OTS, pristine	1,588.3	12.7	2,644.8	29.2	0.12	6.20	7.8×10^{11}
OTS, functionalized	1,596.7	12.4	2,651.1	33.0	0.25	2.66	1.6×10^{12}
hBN, pristine	1,584.7	14.5	2,645.6	27.8	0.13	9.88	8.4×10^{11}
hBN, functionalized	1,595.6	12.1	2,655.8	30.4	0.27	4.51	1.8×10^{12}
Al_2O_3 (sapphire), pristine	1,595.6	12.5	2,653.7	30.7	~0	6.01	~0
Al_2O_3 (sapphire), functionalized	1,598.0	16.3	2,657.6	33.6	1.16	3.31	8.5×10^{12}

Average values for key Raman peak parameters are summarized for pristine and functionalized graphene on SiO_2 (plasma-cleaned), OTS, hBN and Al_2O_3 (sapphire) substrates. The parameters shown are the peak positions of G and 2D peaks (ω_G and ω_{2D}) and FWHM values of G and 2D peaks (Γ_G and Γ_{2D}) and D/G and 2D/G integrated intensity ratios (I_D/I_G and I_{2D}/I_G). The area concentration of defects or reacted sites (σ) is calculated from equation (4).

are summarized in Table 1. Histograms of the I_D/I_G ratio in Fig. 2a show very low initial defect concentrations. After diazonium functionalization, the centres of the distributions have increased to ~1.2 for Al_2O_3 and ~1.4 for SiO_2, indicating a relatively high degree of covalent functionalization. The histograms are also wider, suggesting an increased spatial inhomogeneity. For hBN and OTS, the I_D/I_G ratio has only slightly increased, to ~0.25, indicating much lower reactivity.

Scatter plots of the Raman peak parameters are shown in Fig. 2b–e. Data from literature reports of mechanically exfoliated monolayer graphene doped by electrostatic gating are included on these plots as comparisons[37,41]. In Fig. 2b, the full-width at half-maximum (FWHM) of the G peak (Γ_G) is plotted against the position of the G peak (ω_G). The dashed trend line indicates that increasing n- or p-doping leads to narrowing of the G peak and an increase of the G peak position[36,41,42]. This trend line has been shifted upwards to accommodate the wider G peak in CVD graphene. Pristine graphene on each of the substrates generally follows the doping trend line, with hBN closer to the undoped region and Al_2O_3 closer to the more doped region. However, electron and hole doping cannot be distinguished from this plot, and graphene that is uniformly electron- or hole-doped cannot be distinguished from graphene with many electron- and hole-doped charge puddles. After diazonium functionalization, ω_G is upshifted for all substrates, suggesting increased doping, while Γ_G is also much higher for SiO_2 and Al_2O_3, suggesting increased disorder[43].

The G and 2D peak positions (ω_G and ω_{2D}) are plotted against each other in Fig. 2c together with comparison data[41] to distinguish between n- and p-doping trends. The unfunctionalized graphene in our samples lies in the slightly p-doped region of this plot, with the

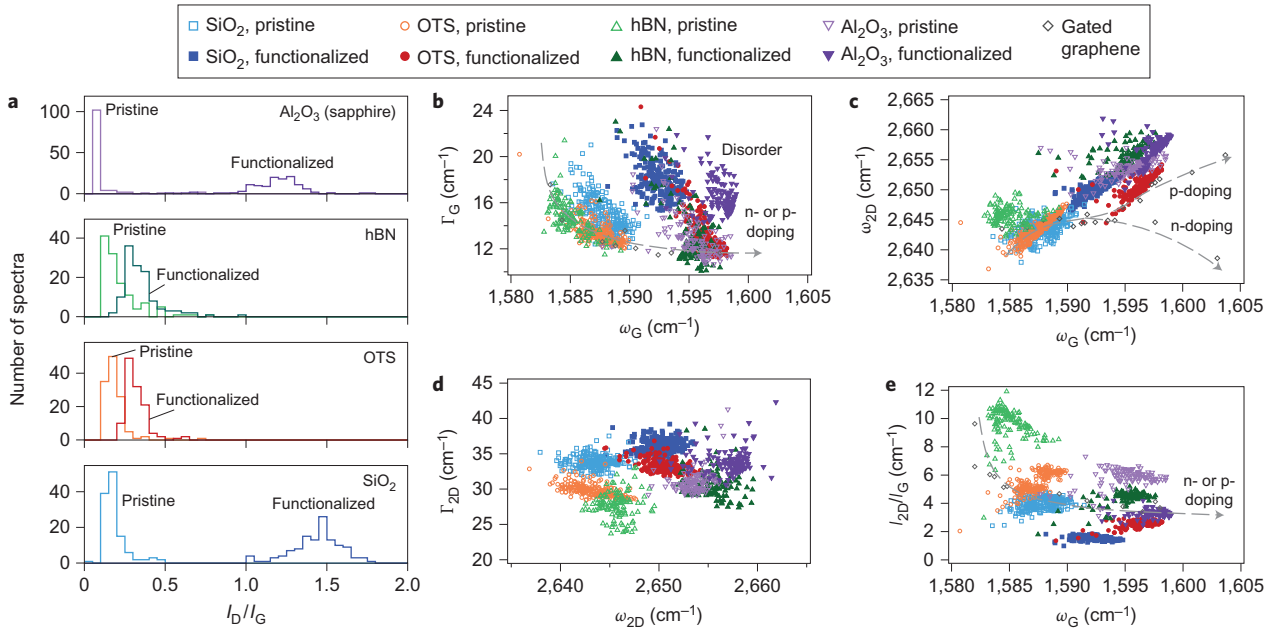

Figure 2 | Raman spectroscopy peak parameter analysis. Spatial Raman maps were collected for graphene supported on each substrate for the same 10 μm × 10 μm regions before and after diazonium functionalization, with 121 spectra in each map. **a**, Histograms of I_D/I_G ratios before and after functionalization. A low degree of covalent functionalization (small increase in I_D/I_G) is seen for OTS and hBN, and a much higher degree for SiO_2 (plasma-cleaned) and Al_2O_3. **b**–**e**, Scatter plots of Raman peak parameters with data points adapted from pristine, mechanically exfoliated graphene doped by electrostatic gating; dashed lines added to guide the eye are included to aid comparison[37,41]. **b**, G peak full-width at half-maximum (FWHM, Γ_G) versus G peak position (ω_G). Comparison data from ref. 41 are shifted up to fit the higher FWHM of CVD graphene. Before reaction, graphene follows the doping trend, but highly functionalized samples significantly deviate above the curve. **c**, 2D peak position (ω_{2D}) versus G peak position (ω_G), with additional data points adapted from ref. 41 for distinguishing n-doped and p-doped exfoliated monolayer graphene, shifted to account for the dependence of ω_{2D} on excitation laser wavelength[56]. Diazonium-functionalized graphene in our experimental data is p-doped, but deviates left from the trend of pristine, gated graphene. **d**, 2D peak FWHM (Γ_{2D}) versus 2D peak position (ω_{2D}), showing clearly distinguished clusters for each substrate before and after functionalization. Increasing Γ_{2D} values before functionalization reflect inhomogeneous broadening due to electron–hole charge fluctuations. **e**, I_{2D}/I_G intensity ratio versus G peak position (ω_G), with comparison data adapted from ref. 37 showing the doping trend. Raman spectra were taken at 633 nm laser excitation wavelength.

hBN surface being less doped, but graphene on Al_2O_3 is on the p-doping branch. After functionalization, graphene on all substrates is further along the p-doping branch. However, covalent defects are expected to cause deviations from these doping-related Raman trends, which were measured on pristine graphene. The p-doping after reaction has contributions from the covalent bond formation itself and from the non-covalent adsorption of the diazonium cation and oligomers[12,13,18]. Strain effects are ruled out as the cause of these peak position shifts because the graphene samples rest conformally on very flat substrates, and mechanical strain causes simultaneous downshifting of both the G and 2D peak positions below the values for undoped graphene[44], instead of the upshift that is observed here.

The FWHM of the 2D peak (Γ_{2D}) is plotted against its position (ω_{2D}) in Fig. 2d. Because the 2D peak position shifts in opposite directions for electron or hole doping (Fig. 2c), the presence of electron–hole puddles with spatial extents significantly smaller than the Raman laser spot size would result in a broadened 2D peak. In our Raman system, the laser spot size is ~0.9 μm in diameter, and the sizes of electron–hole puddles have been measured to be ~5–10 nm in diameter for graphene on SiO_2 and ~100 nm for graphene on hBN[25]. We therefore propose that a higher Γ_{2D} is correlated with higher amplitudes of charge fluctuations. Graphene on SiO_2 exhibits the highest Γ_{2D} values, and graphene on hBN has the lowest. This trend is in general agreement with the amplitudes of charge fluctuations on SiO_2 and hBN measured by scanning tunnelling spectroscopy[25]. On OTS, the Γ_{2D} is slightly higher than on hBN and notably lower than on SiO_2.

The integrated area intensity ratio I_{2D}/I_G is plotted against ω_G in Fig. 2e, with additional comparison data for gated pristine graphene adapted from ref. 37, and shows that the I_{2D}/I_G ratio decreases and ω_G increases for increasing n- and p-doping. Graphene on hBN is closest to the undoped region of the plot, followed by OTS, SiO_2 and finally Al_2O_3 at the more highly doped region. (Although the peak intensities on Al_2O_3 have not been corrected for optical interference effects from the different substrate[45], the peak positions are accurate.) After diazonium functionalization, the data points from all substrates move further along the doping trend line. Again, we observe that diazonium functionalization increases the p-doping of the graphene.

Graphene on the various substrates displays different extents of overall p-doping and apparent intensities of electron–hole charge fluctuations. Graphene on hBN is the least doped, with the lowest degree of charge fluctuations, followed by OTS. In contrast, graphene on SiO_2 and Al_2O_3 are more highly p-doped, and on SiO_2 the Γ_{2D} is the highest, indicating the greatest broadening of the 2D peak from electron–hole puddles. After reaction, graphene on all substrates shows increased p-doping. For the substrates with a low degree of sp^3 hybridization, the p-doping arises from diazonium molecules non-covalently deposited on the graphene. The role of electron–hole puddles in the reactivity of graphene is discussed in the following sections.

Spatial patterning of chemical reactivity. With our RIL technique, a substrate with OTS micropatterned[46,47] on SiO_2 was used to spatially control the chemical reactivity of graphene (Fig. 3a). The patterned surface in the topographic atomic force microscopy (AFM) image of Fig. 3b comprises ~2-μm-wide OTS lines and ~7 μm wide SiO_2 gaps. Graphene was transferred onto this substrate and functionalized by diazonium salts. Figure 3c shows the resulting spatial Raman map of I_D/I_G. The narrower regions of low functionalization correspond to graphene over OTS-covered areas and the wider stripes of high functionalization the SiO_2 regions.

The I_D/I_G spatial profile at the edge of a stripe was fit using an integral Gaussian distribution in Fig. 3d (Supplementary Information, Page 8). The variance of this fit indicates the sharpness of the transition between the on-OTS and on-SiO_2 regions, and is ~0.85 μm. The I_D/I_G profile for graphene across the edge of a flake of hBN is plotted and fitted similarly in Fig. 3e, with a variance of 0.76 μm. These variances are comparable to the 0.71 μm diagonal of the pixel size (0.5 μm × 0.5 μm) and the ~0.9 μm laser spot size. Therefore the measured resolution of the RIL patterns is limited by the optical characterization technique, and the true resolution of the chemical patterning is primarily determined by the spatial resolution of the substrate patterning technique and spatial size of the electron–hole puddles on a given substrate, which the data indicate as less than 1 μm.

Patterned attachment of proteins on graphene. Spatial control of surface chemistry is important for biological applications such as microarrays, biosensors and tissue engineering. Many important macromolecules such as proteins, antibodies or DNA are not compatible with conventional lithographic techniques. RIL allows these biomolecules to be attached to graphene as the final processing step in aqueous solution. The patterning of biomolecules on graphene using RIL is schematically illustrated in Fig. 4a. CVD graphene is transferred to an OTS-patterned substrate and functionalized by 4-carboxybenzenediazonium tetrafluoroborate. The graphene is then reacted with N_α,N_α-bis(carboxymethyl)-L-lysine hydrate (NTA–NH_2) followed by reaction with $NiCl_2$ to complex the Ni^{2+} ions with the NTA structure. Finally, the sample is incubated with a solution of polyhistidine (His)-tagged EGFP to form the graphene–NTA–Ni–His–EGFP complex.

Attachment of the carboxybenzene group is demonstrated by attenuated total reflectance infrared (ATR-IR) spectra of the pristine CVD graphene (blue curve) and functionalized graphene (red curve) in Fig. 4b. Vibrations from carboxyl groups are seen at ~1,730 cm^{-1} (C=O stretching) and ~3,330 cm^{-1} (O–H stretching). Confocal fluorescence microscopy after incubation in EGFP shows bright green stripes, confirming the spatial patterning of the protein tethering reaction (Fig. 4c). The wider, bright lines correspond to graphene resting on SiO_2 where the higher concentration of diazonium attachment sites results in a high coverage of EGFP. The narrower, dark lines correspond to graphene resting on OTS where the low reactivity results in fewer EGFP. The inset shows the fluorescence intensity profile along the white line. This tethering scheme is very robust because of the covalent attachment site, and is also chemically reversible due to the metal ion chelation, in contrast to a previous report of proteins patterned on graphene by physisorption[48].

Reactivity model: the influence of electron puddles. To explain the chemical reactivity of graphene on the different substrates, we use a model describing the reaction kinetics from electron-transfer theory as a function of the Fermi level of graphene and relating the reacted site density to an experimentally measurable Raman I_D/I_G ratio. Owing to the overlap between graphene and the diazonium states, the electron-transfer theory below shows that the reactivity increases for increasingly n-doped graphene and is negligible for p-doped graphene. The schematic in Fig. 5a shows how a graphene sheet that is overall p-doped but with a high electron–hole charge fluctuation amplitude can have much higher reactivity due to the locally n-doped puddles.

In a first-order electron-transfer reaction model, the density of reacted lattice sites σ is given by

$$\sigma = \rho_C(1 - \exp(-(k_{E_T}[D]_S/\rho_C)t)) \quad (1)$$

where ρ_C is the number of carbon atoms per unit area in graphene, $[D]_S$ is the concentration of diazonium ions, k_{ET} is the rate constant of electron transfer, and t is the reaction time. The overall reaction rate is limited by the electron transfer rate from graphene to diazonium, as

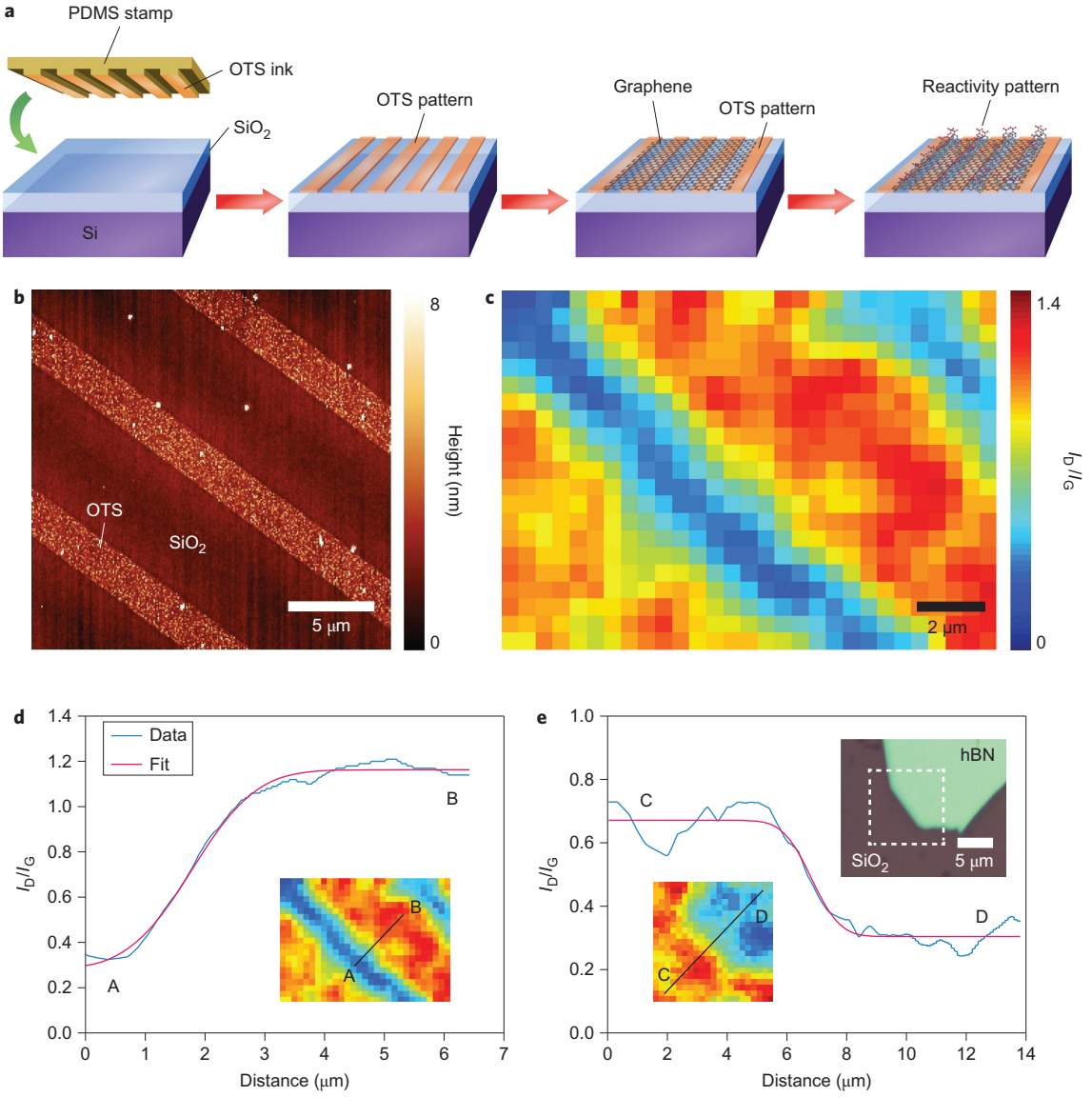

Figure 3 | Spatial control of reactivity of graphene on patterned substrates. a, Schematic illustration of RIL. The SiO_2 substrate is patterned by a PDMS stamp inked with OTS. Graphene is transferred over the OTS-patterned substrate and reacted with 4-NBD tetrafluoroborate. **b**, AFM topographic image of the OTS stripes (narrower raised regions) on SiO_2 before graphene deposition. **c**, Raman spatial map of I_D/I_G intensity ratio after diazonium functionalization. The narrow, mildly functionalized stripes correspond to the regions over the OTS pattern and the wide, strongly functionalized stripes correspond to the regions over the SiO_2 gaps. **d**, Spatial profile of I_D/I_G for the stripe pattern (blue curve) along the line A–B in the Raman map (inset), and a fit to an integrated Gaussian function with a variance of 0.85 μm. **e**, A spatial Raman map (lower left inset) was measured for a region of graphene covering both SiO_2 and a flake of hBN (white box in optical image in upper right inset). The I_D/I_G spatial profile along the line C–D is shown together with the integrated Gaussian fit, which has a variance of 0.76 μm.

is the case for carbon nanotubes[49], and depends on the overlap of states between graphene and diazonium. Once the diazonium radical forms, it is highly reactive and can be quenched readily by a variety of substrates[50,51]. Because the rate-limiting step is electron transfer, the Fermi level of graphene determines the influence of the substrate on graphene reactivity, and the specific interactions of the charged states in graphene with the diazonium radical can be neglected. The rate constant k_{ET} is described using Gerischer–Marcus theory[52]:

$$k_{ET} = \nu_n \int_{E_{redox}}^{E_{F,G}} \varepsilon_{red}(E)\mathrm{DOS}_G(E)W_{ox}(E)\mathrm{d}E \qquad (2)$$

where $E_{F,G} = -4.66$ eV is the Fermi level of undoped graphene, $E_{redox} = -5.15$ eV is the standard potential for the redox couple of the 4-NBD diazonium salt[53] and $\mathrm{DOS}_G(E)$ is the electronic density of states of graphene. The electron-transfer frequency ν_n and integral prefactor ε_{red} are treated as a single fitting parameter $\nu_n\varepsilon_{red}$. The distribution of oxidized states of the solvated diazonium molecule $W_{ox}(E)$ is given by

$$W_{ox}(E) = \frac{1}{\sqrt{4\pi\lambda kT}} \exp\left(-\frac{\left(E - \left(E_{redox} + \lambda\right)\right)^2}{4\lambda kT}\right) \qquad (3)$$

where k is the Boltzmann constant, T is the absolute temperature and λ is the energy difference between the standard potential for the redox couple of the diazonium salt and the energy for maximum probability of finding a vacant state. This parameter is also known as the reorganization energy and is ~0.7 eV for

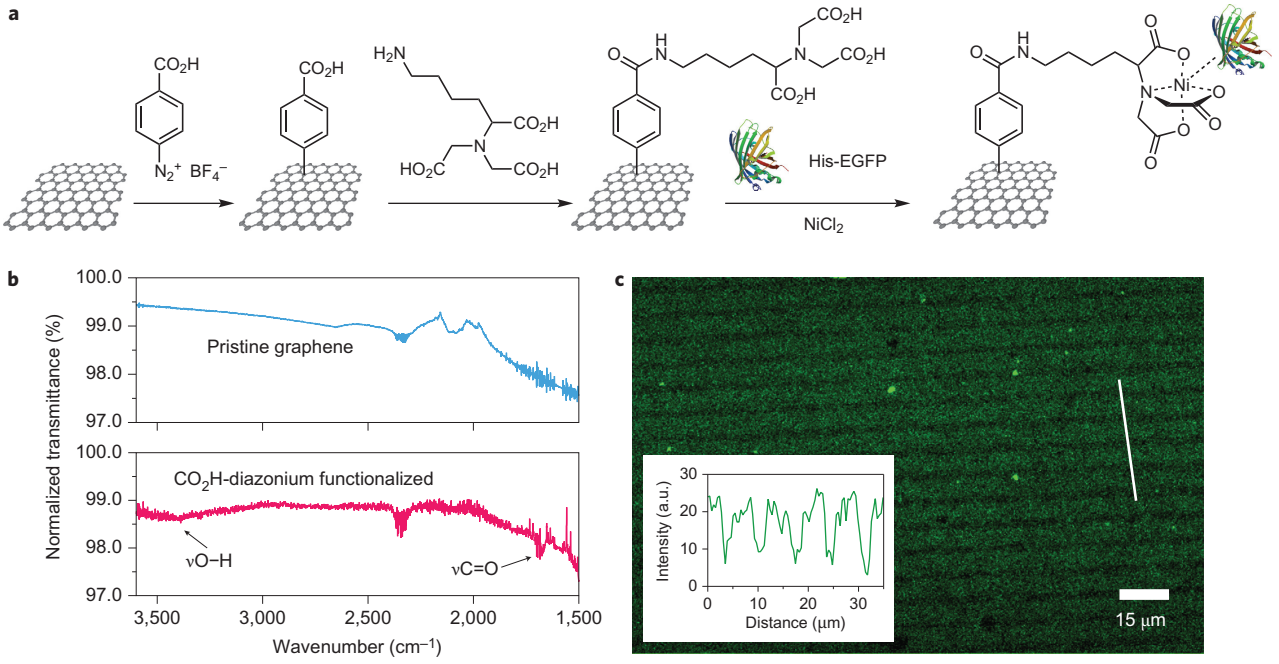

Figure 4 | Patterning of proteins on graphene. a, Schematic illustration of protein-attachment chemistry. The graphene is covalently functionalized with 4-carboxybenzenediazonium tetrafluoroborate, then NTA–NH_2. Reaction with $NiCl_2$ causes Ni^{2+} ions to complex to the covalently attached structures, and link to polyhistidine (His)-tagged EGFP. (Image of EGFP is taken from the RCSB PDB (www.pdb.org) from ref. 57.) **b**, ATR-IR spectra of pristine CVD graphene (blue curve) and CO_2H-diazonium functionalized CVD graphene (red curve), showing O–H and C=O vibrations from the carboxyl groups. **c**, Confocal fluorescence microscope image of EGFP attached to graphene resting on a substrate with alternating stripes of bare SiO_2 and OTS patterned on graphene. The bright green stripes, indicating a higher concentration of EGFP attachment, corresponds to graphene resting on bare SiO_2, and the darker stripes correspond to graphene resting on OTS-patterned regions where very little EGFP was able to attach. Inset: intensity profile of fluorescence along the white line indicated in **c**.

single-walled carbon nanotubes[49]; it is assumed to be similar for graphene. The model here shows how the electronic density of states and Fermi level of graphene directly influence the reaction rate.

The density of reacted sites σ was quantitatively related to the I_D/I_G ratio by Lucchese *et al.*[40]

$$\frac{I_D}{I_G} = C_A \frac{r_A^2 - r_S^2}{r_A^2 - 2r_S^2}\left[\exp\left(-\frac{\pi r_S^2}{L_D^2}\right) - \exp\left(-\frac{\pi\left(r_A^2 - r_S^2\right)}{L_D^2}\right)\right] + C_S\left[1 - \exp\left(-\frac{\pi r_S^2}{L_D^2}\right)\right] \quad (4)$$

where the distance between defects is $L_D = 1/\sqrt{\sigma}$. Around each defect site is a structurally damaged region with radius $r = r_S$ and around that an activated region between $r = r_S$ and $r = r_A$ that is primarily responsible for an increase in the D peak. In ref. 40, changes in I_D/I_G are caused by ion bombardment damage, but covalent functionalization with diazonium salts results in a slightly different behaviour of I_D/I_G (ref. 10). Accordingly, we used smaller values of $r_S = 0.07$ nm and $r_A = 1.0$ nm because a covalent attachment site is much less disruptive to the lattice than an ion bombardment defect. Parameters C_A and C_S are similar to the values used in ref. 40. Combining equations (1) to (4) results in a curve showing the I_D/I_G after diazonium functionalization as a function of graphene E_F with $\nu_n\varepsilon_{red}$ as the fitting parameter. The surface concentration of defect sites σ for graphene on each substrate was estimated from equation (4) and is summarized in Table 1. Our estimated reacted site concentration is $\sim 1 \times 10^{12}$ to $\sim 1 \times 10^{13}$ cm^{-2}, which is much lower than the estimate for near-saturation of 1×10^{15} cm^{-2} reported elsewhere[4], but is consistent with molecularly resolved scanning tunnelling microscopy (STM) of diazonium-functionalized graphene showing a much more sparse coverage[12]. Additional STM imaging as well as Raman spectroscopy would be valuable for clarifying the relation between reacted site concentration and I_D/I_G and for elucidating the graphene microstructure.

The model curve is plotted together with experimental data from several samples of graphene on different substrate materials in Fig. 5b,c. To obtain the average Fermi level, the Raman I_G/I_{2D} ratio was used[54]:

$$\sqrt{\frac{I_G}{I_{2D}}} = C\left(\gamma_{e-ph} + 0.07\left|E_{F,avg}\right|\right) \quad (5)$$

where $\gamma_{e-ph} = \sim 33$ meV is the average energy of electron scattering due to phonon emission and $C \approx 10$ eV^{-1} (ref. 54). We have used the ω_{2D} versus ω_G data (Fig. 2c) to determine $E_{F,avg} < 0$. However, the hole-doped data show little agreement with the model in Fig. 5b. To account for electron–hole puddles as illustrated in Fig. 5a, we note that the reactivity is instead dominated by the sum of the average Fermi level $E_{F,avg}$ and the amplitude of the puddle, which should be proportional to the increase in Γ_{2D} compared to the case with negligible puddle influence. Specifically, the effective Fermi level of the n-doped puddles $E_{F,n}$ is

$$E_{F,n} = E_{F,avg} + \alpha\left(\Gamma_{2D} - \Gamma_{2D,0}\right) \quad (6)$$

where α is a proportionality constant, and $\Gamma_{2D,0}$ is the FWHM of the 2D peak for graphene with no charge puddles. In Fig. 5c, the data points were shifted using $\alpha = 0.08$ eV cm and $\Gamma_{2D,0} = 26$ cm^{-1}, and the model curve is plotted with $\nu_n\varepsilon_{red} = 0.105$. (Note that $\alpha < 0$ for $E_{F,p}$ in the p-doped puddles.) After the adjustment in equation (6) to account for the n-doped puddles, the data are much better described by the model.

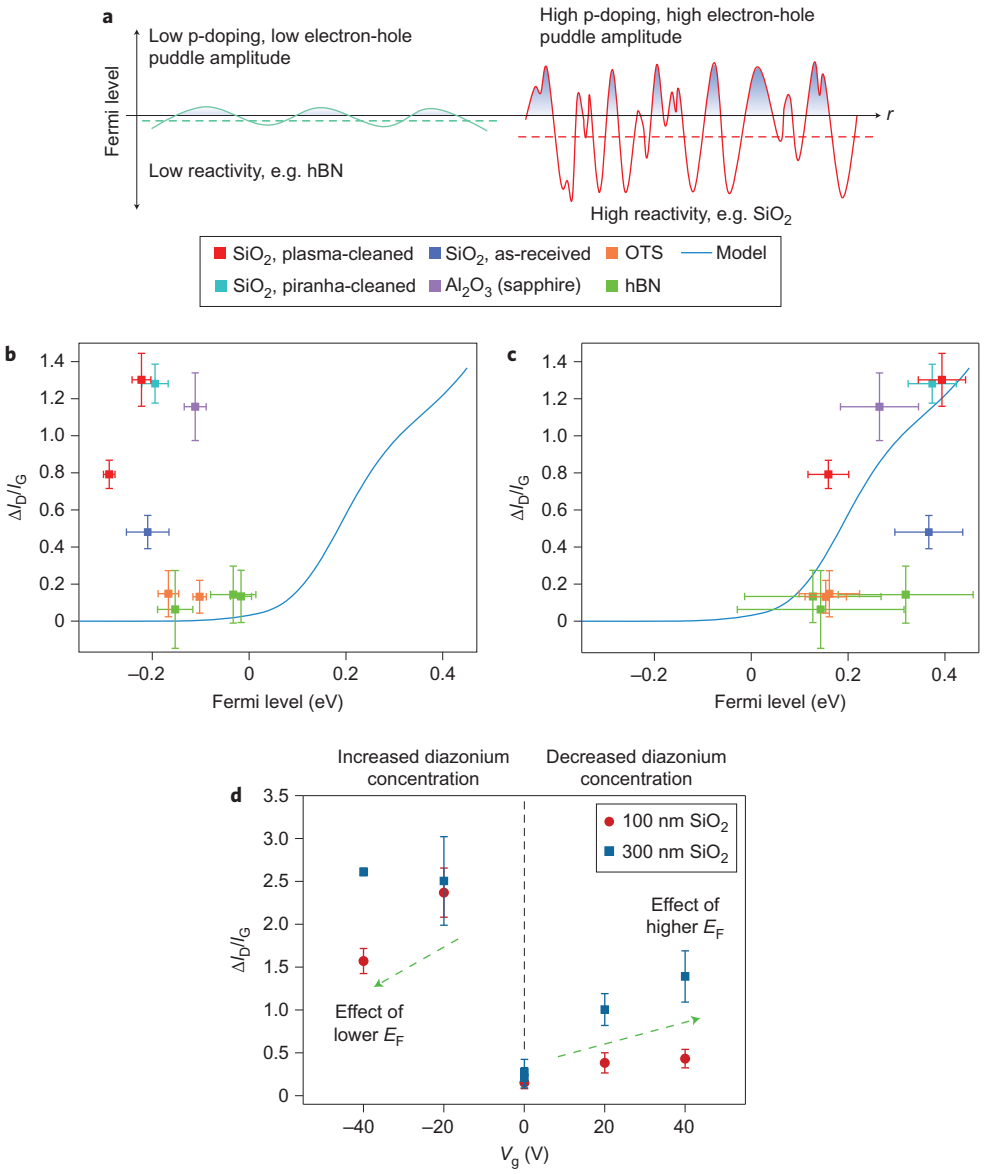

Figure 5 | Modelling of substrate-influenced reactivity. a, Schematic of the role of electron–hole charge fluctuations in graphene reactivity. Solid curves indicate spatial variation of the local Fermi level in charge puddles, and the dashed lines indicate the average Fermi level. The green curve (left) represents graphene on a substrate that causes it to be mildly p-doped with small charge fluctuations, and the red curve (right) represents higher p-doping and large charge fluctuations. According to electron-transfer theory, n-doped puddles have a higher reactivity towards diazonium functionalization and the p-doped puddles have very low reactivity. **b**, Experimental data from graphene on various substrates are plotted together with the curve from the electron-transfer model for the initial graphene Fermi level (E_F) and change in I_D/I_G ratio after diazonium functionalization. The experimental average E_F values are calculated from the I_{2D}/I_G ratios before functionalization[37]. Each experimental point is the average value for a particular sample taken from 121 Raman spectra in a map, and the error bars represent standard deviation. The average doping for all samples is p-type, and does not agree with the model. **c**, Average E_F values are offset by considering the FWHM of 2D peaks, which reflects inhomogeneous broadening due to electron–hole charge fluctuations, to reflect the maximum n-doping. **d**, Resulting I_D/I_G ratio changes measured after electrochemical functionalization experiments at different applied gate voltages for samples on 100 nm and 300 nm SiO_2 dielectric layers, showing the effect of Fermi level shifts and field-induced diazonium concentration change on overall reactivity.

Considering the Raman spectral analysis and the modelling results above, we can summarize the effects of the different substrates on the chemical reactivity of graphene. Graphene on hBN and OTS has low electron–hole fluctuations and hence lower diazonium reactivity, whereas graphene on hydrophilic SiO_2 (plasma-cleaned and piranha-cleaned) and Al_2O_3 has higher charge fluctuations that result in more n-doped reactive regions. The charge fluctuations on SiO_2 are caused by charged impurities in the substrate and polar adsorbates on the surface, so adding the OTS monolayer decreases the fluctuations by increasing the distance between the graphene and the charged impurities and by reducing the adsorption of polar adsorbates such as water. An unknown film of organic contamination probably covers as-received SiO_2 substrates and serves a similar role as the OTS monolayer. Although the Al_2O_3 substrates are single crystals in the bulk, their surfaces are likely to be similar to the amorphous SiO_2 substrates.

The Fermi level offsets calculated in equation (6) are larger than the electron–hole fluctuations reported earlier for mechanically exfoliated single-crystal graphene[25]. This difference may be explained by grain boundaries and other contaminants in the CVD graphene that can increase the reactivity for a lower Fermi level shift. Furthermore, the 2D Raman peaks from graphene with high electron–hole fluctuations would also have lower intensities,

causing the $E_{F,avg}$ calculated from equation (5) to be further from neutrality and requiring a larger shift in equation (6) to fit the I_D/I_G. The hydrophobicity of the substrate is an initial predictor of the chemical reactivity as shown in Fig. 1c because the surface energy of the substrate relates to the presence of charged impurities and polar surface groups that can induce electron–hole charge fluctuations in graphene.

To test the implications of our substrate-dependent graphene reactivity results and model, we conducted electrochemical functionalization experiments where the graphene was electrically doped by an applied backgate voltage during reaction (see full details in the Supplementary Information, Pages 10–13 and Supplementary Fig. S8). Our model suggests that for sufficiently large shifts in the Fermi level, the contribution of the electron–hole puddles is overcome by the overall Fermi level, with overall reactivity decreasing for overall highly p-doped graphene and increasing for overall highly n-doped graphene. This approach is complicated by the diazonium cation being either attracted or repelled by the applied gate voltage so that the concentration of diazonium at the graphene surface is significantly increased or decreased. This concentration effect at the ionic double layer near the graphene surface saturates with electric field, so comparisons can still be made between reactions at different electric field strengths in each of these limits. In Fig. 5d, the resulting I_D/I_G ratios are plotted as a function of gate voltage during reaction on two different SiO_2 layer thicknesses (100 nm and 300 nm) to compare the effect of different electric field strengths. At positive gate voltage, reactivity is higher due to the higher Fermi level, as expected, even though the diazonium concentration at the graphene surface is lower. At negative gate voltage, the increase in diazonium concentration dominates and causes a significantly increased reactivity. However, for the highest negative fields, occurring with the thinner dielectric layer, the diazonium concentration can be seen to saturate and the p-doping of the graphene begins to decrease the reactivity as expected. These experiments therefore support the electron-transfer rate model developed above. Additional exploration of electrochemical functionalization will provide further insight into this reaction mechanism.

Conclusions

In summary, the effect of the underlying substrate on the chemical reactivity of graphene has been explored using detailed Raman spectroscopy. Graphene on SiO_2 and Al_2O_3 is more reactive towards covalent functionalization by aryl diazonium salts than graphene on hBN or on an alkyl-terminated monolayer. The reactivity contrast is attributed to higher amplitudes of the substrate-induced electron–hole charge fluctuations for graphene on SiO_2 and Al_2O_3. Micrometre-scale spatial control of the chemical reactivity of graphene was demonstrated by chemically patterning the substrate before deposition of graphene. Owing to the versatility and chemical tailorability of the RIL technique, it can be used for the modification and manipulation of graphene. This chemical patterning technique was also applied to the spatial patterning of protein molecules on graphene, demonstrating the potential for applications in biosensing.

Methods

Graphene synthesis and transfer. Copper foil substrates (25 μm, 99.8%, Alfa Aesar) were annealed under a hydrogen atmosphere (1,000 °C, 30 min, 10 s.c.c.m. hydrogen, ~330 mtorr total pressure) followed by graphene synthesis with methane (1,000 °C, 40 min, 15 s.c.c.m. methane and 50 s.c.c.m. hydrogen, ~1.5 torr total pressure). Graphene on copper was coated in PMMA (950PMMA, A4, MicroChem) by spin-coating (3,000 r.p.m., 1 min), then dried in air (30 min). Graphene on the reverse side was removed by reactive ion etching (Plasmatherm RIE, 100 W, 7 mtorr oxygen, 5 min). The PMMA–graphene–copper stack was placed on the surface of copper etchant (6 M HCl and 1 M $CuCl_2$ in water). After copper etching (~30 min), the PMMA–graphene layer was scooped out with a clean wafer and floated on several baths of ultrapure water for rinsing. It was then scooped out with the target substrate and dried in air overnight before immersion in several baths of clean acetone to dissolve the PMMA, followed by rinsing in isopropanol and drying with nitrogen gas.

Surface preparation of wafer substrates. Silicon wafers with 300 nm SiO_2 were ultrasonically cleaned in sequential baths of acetone and isopropanol, blown dry with nitrogen, and subjected to additional surface treatments. *Plasma-cleaned samples*: these were exposed to oxygen plasma (AutoGlow Plasma System, Glow Research) for 10–30 min at 200 W power and 0.5 torr. *Piranha-cleaned samples*: these were immersed in piranha solution (3:1 solution of sulfuric acid and 30% hydrogen peroxide) for 15 min and rinsed in ultrapure water. (Warning: piranha solution is a strong oxidizing agent and should be handled with extreme care.) *As-received samples*: these were subjected to no additional treatment. Sapphire wafers (α-Al_2O_3, *c*-plane, 0.5 mm thick, MTI Corp.) were ultrasonically cleaned in acetone and isopropanol and blown dry with nitrogen.

OTS monolayer on SiO_2. Octadecyltrichlorosilane (OTS) (Sigma-Aldrich, 90+%) SAMs were formed on freshly plasma-cleaned SiO_2 substrates in OTS solution (10 mM in toluene) overnight in a closed vial, then rinsed in fresh toluene and blown dry with nitrogen.

Surface patterning of substrates. OTS patterns were formed on freshly plasma-cleaned SiO_2 substrates by printing with polydimethylsiloxane (PDMS) stamps. Master patterns were formed by electron-beam lithography of PMMA resists on silicon wafers. PDMS (10:1 mass ratio of base to curing agent, Dow Corning Sylgard 184) was poured into the master patterns, degassed in vacuum for 45 min, and cured at 100 °C for 2 h on a hotplate. The stamps were inked by spin-coating 10 mM OTS in anhydrous toluene (3,000 r.p.m., 30 s), then gently brought into contact with the substrates for 60 s.

hBN preparation. The hBN flakes used in this study were prepared by mechanical exfoliation of an ultrapure single crystal of hBN on piranha-cleaned SiO_2/silicon substrates. The hBN crystal was grown using a method described previously[55].

Diazonium functionalization of graphene. Graphene samples supported on substrates were immersed in aqueous solutions of 10 mM 4-NBD tetrafluoroborate and 0.5 wt% sodium dodecyl sulfate (SDS) with constant stirring at ~35 °C. Most samples were reacted for 16.5 h to reach full reaction conversion (the sample in Fig. 4 was reacted for 1.5 h to improve I_D/I_G spatial contrast). After reaction, samples were rinsed in ultrapure water and blown dry with nitrogen. NMR and optical absorbance spectroscopies were used to verify diazonium stability (Supplementary Fig. S6).

Raman spectroscopy and mapping. Raman spectroscopy was performed on a Horiba Jobin Yvon LabRAM HR800 system using a 633 nm excitation laser, ×100 objective lens with ~1-μm-diameter spot size and a motorized *XYZ* stage. The G, 2D and D peaks were fit to Lorentzian functions.

Contact angle. The contact angles of the substrates were measured using a Ramé–Hart goniometer and 2 μl sessile droplets of ultrapure water. Several droplets were measured in different sample locations and the results were averaged.

Atomic force microscopy. AFM imaging was conducted on an Asylum Research MFP-3D system in a.c. (non-contact) mode using silicon probes (Olympus OMCL-AC240TS). Images were processed using the Gwyddion software package.

Binding of proteins on graphene. Graphene samples on OTS-patterned SiO_2 substrates were immersed in an aqueous solution of 1 wt% SDS and 50 μM 4-carboxybenzenediazonium tetrafluoroborate and stirred at 45 °C for 12 h. They were then immersed in a phosphate buffered solution (pH 8.3) with 100 μM of (NTA–NH_2) at room temperature for 8 h, followed by an aqueous solution of 20 μM $NiCl_2$ at room temperature for 4 h to complex the Ni^{2+} ions to the NTA structure. They were then immersed in an aqueous solution of 1 μM polyhistidine (His)-tagged EGFP at room temperature for 1 h. Between each step above, the sample was rinsed with water, acetone and isopropanol and blown dry with nitrogen. ATR-IR spectra were obtained using a Thermo Nicolet 4700 spectrometer. Confocal fluorescence microscopy images were captured using a Zeiss LSM 710 NLO with 633 nm laser excitation.

Received 30 January 2012; accepted 27 June 2012; published online 12 August 2012

References

1. Geim, A. K. Graphene: status and prospects. *Science* **324,** 1530–1534 (2009).
2. Novoselov, K. S. *et al.* Electric field effect in atomically thin carbon films. *Science* **306,** 666–669 (2004).
3. Rao, C. N. R., Sood, A. K., Subrahmanyam, K. S. & Govindaraj, A. Graphene: the new two-dimensional nanomaterial. *Angew. Chem. Int. Ed.* **48,** 7752–7777 (2009).
4. Bekyarova, E. *et al.* Chemical modification of epitaxial graphene: spontaneous grafting of aryl groups. *J. Am. Chem. Soc.* **131,** 1336–1337 (2009).
5. Elias, D. C. *et al.* Control of graphene's properties by reversible hydrogenation: evidence for graphane. *Science* **323,** 610–613 (2009).

6. Wang, Q. H. & Hersam, M. C. Nanofabrication of heteromolecular organic nanostructures on epitaxial graphene via room temperature feedback-controlled lithography. *Nano Lett.* **11,** 589–593 (2010).
7. Chen, W., Chen, S., Qi, D. C., Gao, X. Y. & Wee, A. T. S. Surface transfer p-type doping of epitaxial graphene. *J. Am. Chem. Soc.* **129,** 10418–10422 (2007).
8. Wang, Q. H. & Hersam, M. C. Room-temperature molecular-resolution characterization of self-assembled organic monolayers on epitaxial graphene. *Nature Chem.* **1,** 206–211 (2009).
9. Jin, Z. *et al.* Click chemistry on solution-dispersed graphene and monolayer CVD graphene. *Chem. Mater.* **23,** 3362–3370 (2011).
10. Niyogi, S. *et al.* Spectroscopy of covalently functionalized graphene. *Nano Lett.* **10,** 4061–4066 (2010).
11. Sharma, R., Baik, J. H., Perera, C. J. & Strano, M. S. Anomalously large reactivity of single graphene layers and edges toward electron transfer chemistries. *Nano Lett.* **10,** 398–405 (2010).
12. Hossain, M. Z., Walsh, M. A. & Hersam, M. C. Scanning tunneling microscopy, spectroscopy, and nanolithography of epitaxial graphene chemically modified with aryl moieties. *J. Am. Chem. Soc.* **132,** 15399–15403 (2010).
13. Farmer, D. B. *et al.* Chemical doping and electron–hole conduction asymmetry in graphene devices. *Nano Lett.* **9,** 388–392 (2009).
14. Lomeda, J. R., Doyle, C. D., Kosynkin, D. V., Hwang, W. F. & Tour, J. M. Diazonium functionalization of surfactant-wrapped chemically converted graphene sheets. *J. Am. Chem. Soc.* **130,** 16201–16206 (2008).
15. Sinitskii, A. *et al.* Kinetics of diazonium functionalization of chemically converted graphene nanoribbons. *ACS Nano* **4,** 1949–1954 (2010).
16. Englert, J. M. *et al.* Covalent bulk functionalization of graphene. *Nature Chem.* **3,** 279–286 (2011).
17. Farmer, D. B., Lin, Y. M., Afzali-Ardakani, A. & Avouris, P. Behavior of a chemically doped graphene junction. *Appl. Phys. Lett.* **94,** 213106 (2009).
18. Fan, X. Y., Nouchi, R., Yin, L. C. & Tanigaki, K. Effects of electron-transfer chemical modification on the electrical characteristics of graphene. *Nanotechnology* **21,** 475208 (2010).
19. Zhang, H. *et al.* Aryl functionalization as a route to band gap engineering in single layer graphene devices. *Nano Lett.* **11,** 4047–4051 (2011).
20. Chen, J. H. *et al.* Charged-impurity scattering in graphene. *Nature Phys.* **4,** 377–381 (2008).
21. Zhang, Y., Brar, V. W., Girit, C., Zettl, A. & Crommie, M. F. Origin of spatial charge inhomogeneity in graphene. *Nature Phys.* **5,** 722–726 (2009).
22. Du, X., Skachko, I., Barker, A. & Andrei, E. Y. Approaching ballistic transport in suspended graphene. *Nature Nanotech.* **3,** 491–495 (2008).
23. Bolotin, K. I. *et al.* Ultrahigh electron mobility in suspended graphene. *Solid State Commun.* **146,** 351–355 (2008).
24. Dean, C. R. *et al.* Boron nitride substrates for high-quality graphene electronics. *Nature Nanotech.* **5,** 722–726 (2010).
25. Xue, J. M. X. J. M. *et al.* Scanning tunnelling microscopy and spectroscopy of ultra-flat graphene on hexagonal boron nitride. *Nature Mater.* **10,** 282–285 (2011).
26. Lafkioti, M. *et al.* Graphene on a hydrophobic substrate: doping reduction and hysteresis suppression under ambient conditions. *Nano Lett.* **10,** 1149–1153 (2010).
27. Liu, Z. H., Bol, A. A. & Haensch, W. Large-scale graphene transistors with enhanced performance and reliability based on interface engineering by phenylsilane self-assembled monolayers. *Nano Lett.* **11,** 523–528 (2011).
28. Yokota, K., Takai, K. & Enoki, T. Carrier control of graphene driven by the proximity effect of functionalized self-assembled monolayers. *Nano Lett.* **11,** 3669–3675 (2011).
29. Yan, Z. *et al.* Controlled modulation of electronic properties of graphene by self-assembled monolayers on SiO_2 substrates. *ACS Nano* **5,** 1535–1540 (2011).
30. Fan, X., Nouchi, R. & Tanigaki, K. Effect of charge puddles and ripples on the chemical reactivity of single layer graphene supported by SiO_2/Si substrate. *J. Phys. Chem. C* **115,** 12960–12964 (2011).
31. Li, X. *et al.* Large-area synthesis of high-quality and uniform graphene films on copper foils. *Science* **324,** 1312–1314 (2009).
32. Reina, A. *et al.* Large area, few-layer graphene films on arbitrary substrates by chemical vapor deposition. *Nano Lett.* **9,** 30–35 (2008).
33. Huang, P. Y. *et al.* Grains and grain boundaries in single-layer graphene atomic patchwork quilts. *Nature* **469,** 389–392 (2011).
34. Kim, K. *et al.* Grain boundary mapping in polycrystalline graphene. *ACS Nano* **5,** 2142–2146 (2011).
35. Ferrari, A. C. *et al.* Raman spectrum of graphene and graphene layers. *Phys. Rev. Lett.* **97,** 187401 (2006).
36. Ferrari, A. C. Raman spectroscopy of graphene and graphite: disorder, electron–phonon coupling, doping and nonadiabatic effects. *Solid State Commun.* **143,** 47–57 (2007).
37. Basko, D. M., Piscanec, S. & Ferrari, A. C. Electron–electron interactions and doping dependence of the two-phonon Raman intensity in graphene. *Phys. Rev. B* **80,** 165413 (2009).
38. Cançado, L. G. *et al.* Quantifying defects in graphene via Raman spectroscopy at different excitation energies. *Nano Lett.* **11,** 3190–3196 (2011).
39. Ferrari, A. C. & Robertson, J. Interpretation of Raman spectra of disordered and amorphous carbon. *Phys. Rev. B* **61,** 014095 (2000).
40. Lucchese, M. M. *et al.* Quantifying ion-induced defects and Raman relaxation length in graphene. *Carbon* **48,** 1592–1597 (2010).
41. Das, A. *et al.* Monitoring dopants by Raman scattering in an electrochemically top-gated graphene transistor. *Nature Nanotech.* **3,** 210–215 (2008).
42. Lazzeri, M. & Mauri, F. Nonadiabatic Kohn anomaly in a doped graphene monolayer. *Phys. Rev. Lett.* **97,** 266407 (2006).
43. Casiraghi, C. Probing disorder and charged impurities in graphene by Raman spectroscopy. *Phys. Status Solidi RRL* **3,** 175–177 (2009).
44. Mohiuddin, T. M. G. *et al.* Uniaxial strain in graphene by Raman spectroscopy: G peak splitting, Gruneisen parameters, and sample orientation. *Phys. Rev. B* **79,** 205433 (2009).
45. Yoon, D. *et al.* Interference effect on Raman spectrum of graphene on SiO_2/Si. *Phys. Rev. B* **80,** 125422 (2009).
46. Qin, D., Xia, Y. & Whitesides, G. M. Soft lithography for micro- and nanoscale patterning. *Nature Protoc.* **5,** 491–502 (2010).
47. Xia, Y., Mrksich, M., Kim, E. & Whitesides, G. M. Microcontact printing of octadecylsiloxane on the surface of silicon dioxide and its application in microfabrication. *J. Am. Chem. Soc.* **117,** 9576–9577 (1995).
48. Kodali, V. K. *et al.* Nonperturbative chemical modification of graphene for protein micropatterning. *Langmuir* **27,** 863–865 (2010).
49. Nair, N., Kim, W.-J., Usrey, M. L. & Strano, M. S. A structure–reactivity relationship for single walled carbon nanotubes reacting with 4-hydroxybenzene diazonium salt. *J. Am. Chem. Soc.* **129,** 3946–3954 (2007).
50. Mahouche-Chergui, S., Gam-Derouich, S., Mangeney, C. & Chehimi, M. M. Aryl diazonium salts: a new class of coupling agents for bonding polymers, biomacromolecules and nanoparticles to surfaces. *Chem. Soc. Rev.* **40,** 4143–4166 (2011).
51. Galli, C. Radical reactions of arenediazonium ions: an easy entry into the chemistry of the aryl radical. *Chem. Rev.* **88,** 765–792 (1988).
52. Bard, A. J. & Faulkner, L. R. *Electrochemical Methods: Fundamentals and Applications* 2nd edn (Wiley, 2001).
53. Sharma, R., Nair, N. & Strano, M. S. Structure–reactivity relationships for graphene nanoribbons. *J. Phys. Chem. C* **113,** 14771–14777 (2009).
54. Casiraghi, C. Doping dependence of the Raman peaks intensity of graphene close to the Dirac point. *Phys. Rev. B* **80,** 233407 (2009).
55. Taniguchi, T. & Watanabe, K. Synthesis of high-purity boron nitride single crystals under high pressure by using Ba–BN solvent. *J. Cryst. Growth* **303,** 525–529 (2007).
56. Thomsen, C. & Reich, S. Double resonant Raman scattering in graphite. *Phys. Rev. Lett.* **85,** 5214–5217 (2000).
57. Royant, A. & Noirclerc-Savoye, M. Stabilizing role of glutamic acid 222 in the structure of enhanced green fluorescent protein. *J. Struct. Biol.* **174,** 385–390 (2011).

Acknowledgements

This work was primarily funded by a 2009 US Office of Naval Research Multi University Research Initiative (MURI) grant on Graphene Advanced Terahertz Engineering (GATE) at MIT, Harvard and Boston University. J.D.S.-Y. and P.J.-H. acknowledge support from an NSF CAREER award (DMR-0845287). K.K.K. acknowledges an NSF award (DMR-0845358) and support from the Materials, Structures and Device (MSD) Center of the Focus Center Research Program (FCRP) at the Semiconductor Research Corporation. The authors thank M.K. Mondol of the MIT Scanning Electron Beam Lithography facility for assistance.

Author contributions

Q.H.W. designed and conducted the substrate and patterning experiments, performed Raman spectroscopy, AFM and data analysis. Z.J. performed protein attachment, ATR–IR and fluorescence imaging. A.J.H., Q.H.W. and M.S.S. devised the model. K.K.K. synthesized the CVD graphene. K.W. and T.T. synthesized the hBN crystal. J.D.S.-Y. exfoliated the hBN crystal. G.L.C.P., C.-J.S. and M.-H.H. conducted additional experiments. Q.H.W. and M.S.S. wrote the manuscript. All authors contributed to the discussion and interpretation of results.

Additional information

The authors declare no competing financial interests. Supplementary information accompanies this paper at www.nature.com/naturechemistry. Reprints and permission information is available online at http://www.nature.com/reprints. Correspondence and requests for materials should be addressed to M.S.S.